ORIGINAL ARTICLE

Effect of coarse grain matrix content on the mechanical behavior of trimodaled AA 6061-TiO₂ nanocomposite prepared by mechanical alloying

S. Sivasankaran · K. Sivaprasad · R. Narayanasamy ·
M. Saravanan

Abstract In the present work, nanocrystalline AA 6061 alloy powders reinforced with fine titania particles were mechanically blended with coarse-grain AA 6061 alloy powders to produce a trimodal microstructure. The nanocrystallite and trimodaled composite powders were consolidated by cold uniaxial compaction, followed by sintering under controlled atmosphere. The microstructural features for the developed trimodaled composite were evaluated using an optical microscope, a scanning electron microscope, and a transmission electron microscope. The mechanical behavior of these consolidates were evaluated at room temperature. It was observed that trimodal bulk nanocomposite had exhibited balanced mechanical properties of enhanced yield strength and improved ductility compared to nanocrystallite composite.

Keywords Metal matrix composites · Mechanical alloying · Trimodal · Mechanical behavior

S. Sivasankaran (✉)
School of Mechanical and Industrial Engineering, HAWASSA University, Hawassa, Ethiopia
e-mail: sivasankarangs1979@gmail.com

K. Sivaprasad
Department of Metallurgical and Materials Engineering, National Institute of Technology, Tiruchirappalli 620015, India
e-mail: ksp@nitt.edu

R. Narayanasamy
Department of Production Engineering, National Institute of Technology, Tiruchirappalli 620015, India
e-mail: narayan@nitt.edu

M. Saravanan
Powder Metallurgy Shop, Heavy Alloy Penetrator Project, Tiruchirappalli 620025, India
e-mail: srilakspriya@gmail.com

1 Introduction

Controllable properties through appropriate selection of alloy composition and processing method can be obtained through metal matrix composites (MMCs). MMCs resulting from the addition of reinforcements to a metal or alloy may provide enhanced specific strength, stiffness with improved fatigue and wear resistance, and improved thermal properties [1–4]. Aluminum is the most abundant metal in the earth's crust next to iron ore. Its widespread use is due to qualities which include high strength-to-weight ratio, corrosion resistance, high electrical conductivity, easy fabrication, high thermal conductivity, high toughness at cryogenic temperatures, reflectivity, non-toxicity, and recyclability [5]. Among all the Al alloys, Al 6061 possesses excellent formability, weldability, and machinability in addition to high strength, good corrosion resistance, and low cost [6, 7]. Hence, Al 6061 was selected as a matrix material for the present investigation.

In recent years, new methods of manufacturing processes have been developed to produce MMCs that give composites with higher properties or even to maintain the same level of properties at lower cost [8]. The powder metallurgy (P/M) process can produce MMCs in the whole range of matrix reinforcement compositions without the segregation phenomena that occur in the case of casting processes [9–12]. An excellent combination of properties can be achieved by Al-based alloy which have very attractive properties for aerospace, electronics, automotive, and structural applications. It is well known that the addition of ceramic hard particles (e.g., Al_2O_3, TiO_2, SiC_p, etc.) to soft Al alloys increases the strength at ambient and elevated temperatures and wear resistance. The ceramics in the form of oxides, carbides, nitrides, etc., are the most frequently used reinforcement materials (SiC_p, Al_2O_3, TiB_2, B_4C, and graphite). Work on P/M aluminum alloy-based composites reinforced by ceramic particles such as graphite, SiCp, Al_2O_3, TiC, VC, AlN, B_4C, Si_3N_4, TiB_2, AlB_2, ZrC,

and MgB_2 has been successfully dispersed and investigated via mechanical alloying/mechanical milling (MA/MM). There is no reported study concerning TiO_2 powders used as a reinforcement in Al-based MMCs. Titania (TiO_2) has outstanding properties such as high mechanical hardness, thermal stability at high temperatures, good wear and corrosion resistance, low coefficient of thermal expansion, thermal shock resistance, and more excellent catalytic performance [6, 13, 14].

To facilitate the prevention of reinforcement clusters or agglomerates on the matrix, especially in the case of small-sized reinforcement particles, mechanical alloying (MA) is one of the P/M processes that produce uniform dispersion of the reinforcement particles in the matrix. Also, it is one of the leading production methods to produce nanostructured materials. The mechanical alloying process is a high-energy ball milling technique which produces materials at nanometric level. The process of MA/MM is based on imparting a severe plastic deformation on the powder using high-energy ball milling technique. Using this method, an extremely high strain is imparted on the material, and structural refinement occurs by shear and fracture of phase mixtures and by re-crystallization processes with a given phase. Severe plastic deformation can lead to obtaining an as-fine-as-nano-grain structure. The MA process consists of repeated welding–fracturing–welding of a mixture of powder particles in a high-energy ball mill [15–17].

Enhanced mechanical properties especially for strength can be achieved in nanocrystalline (NC) materials due to grain refinement. However, the NC or nanocomposite materials generally exhibit poor ductility and toughness [18]. Based on Hall–Petch relationship, with decreasing grain size, the strength increases by sacrificing ductility [19, 20]. Therefore, in order to restore the ductility of NC materials, various approaches are addressed [21, 22] viz.: (1) introducing coarse-grain (CG) microstructure in NC materials, called bimodal grain microstructure, which facilitates dislocation activity, and (2) annealing of the NC materials that promote grain growth which results in strength degradation. It is well known that the introduction of the ceramic phase will further increase the mechanical strength of the NC materials, resulting in further reduction of ductility and which limits the use of nanocomposites in structural applications. Recently, a trimodal Al-based composite consisting of NC Al phase reinforced with boron carbide (B_4C) along with CG Al phase embedded in the matrix has been successfully fabricated by various authors [23, 24]. It was reported that the trimodal Al-based metal matrix composites produced by cryomilling followed by blending exhibited extremely high compressive yield strength and tailorable ductility. The properties of trimodal Al-based metal matrix composites are influenced by several microstructural features [24–27] such as (1) volume or weight fraction of CG and NC matrix and dispersoids, (2)

particle size and distribution of dispersoids in the matrix, (3) grain size of NC matrix, (4) size and distribution of CG bands in NC matrix, and (5) dislocation densities in the NC and CG domains. A schematic diagram of incorporating CG into nanostructured materials before and after compression is shown in Fig. 1.

The main objective of the present work is to introduce varying fractions of CG AA 6061 alloy phase into the NC AA 6061 composite with 10 wt.% TiO_2 reinforcement by mechanical alloying (MA) to develop a lightweight material with improved strength and ductility. The microstructure and mechanical properties of the trimodal AA 6061-TiO_2 composite were explained in this study. The material selected as AA 6061-TiO_2 particulate MMCs was mainly proposed for aircraft and automotive parts such as aircraft fittings, couplings, marine fittings, electrical fittings, contactors, brake pistons, hydraulic pistons, valves and valve parts, bike frames, bicycle hub, automotive engine pistons, and connecting rod.

2 Experimental procedure

The chemical composition of AA 6061 Al-alloy produced from pure elemental powders (average particle size, 40 μm) is 99.68Al-0.68Si-0.7Fe-0.275Cu-0.15Mn-1Mg-0.195Cr-0.25Zn-0.15Ti (wt.%). Very fine titania (TiO_2, anatase form with tetragonal structure, <1 μm average particle size, 3.84 g/cm^3 density, supplied by Alfa Acer) particles were used as dispersoids to make composite powders. The chemical composition and powder size of the pure elemental powders used in this study to make AA 6061 Al alloy matrix are also given in Table 1. The AA 6061-10 wt.% TiO_2 nanocomposite powder was synthesized via mechanical alloying. The MA was carried out using a planetary ball mill (Insmart systems, Hyderabad, India) in toluene at 280 rpm with a ball-to-powder ratio of 10:1 (hardened stainless steel media) and milled up to 40 h to ensure that the process has reached its steady state. Figure 2a, c shows the morphologies of as-received Al and TiO_2 powder particles, respectively, using secondary electron image of scanning electron micrograph (SE-SEM). From Fig. 2a, c, it can be observed that the Al matrix powder particles were in irregular-flake-like shape, and TiO_2 particles were in clustered tetragonal shape. Figure 2b, d shows the X-ray diffraction patterns of as-received Al and TiO_2 particles, respectively, which indicate the well crystalline nature of the powders. The as-received TiO_2 particles are in anatase form and tetragonal structure with average clustered particles in the size of less than 1 μm, which was measured by laser scattering system technique. The mechanically alloyed (MAed) nanocomposite powders were homogeneously blended with different weight percentages of 0, 5, 10, 15, 20, 25, and 30 % CG AA 6061 matrix powders in the same planetary ball mill with BPR of 1:1 (ϕ 6 mm stainless steel balls) at 120 rpm mixed up

Fig. 1 Schematic representation of incorporating coarse-grain powders to improve the ductility of nanocrystalline materials **a** before compression and **b** after compression
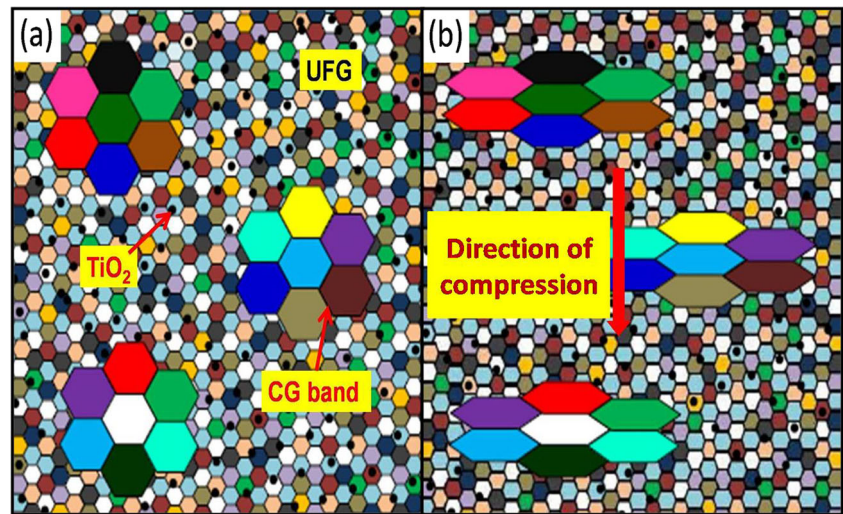
to 4 h to get a trimodal microstructure distribution. The trimodal composite powder consists of CG alloy phase along with hard titania phase reinforced within the matrix of NC Al-alloy. The trimodal composite powders were dried and stress-relieved at 343 K for 1 h under N_2 atm.

These powders were subjected to cold compaction at 500 MPa (using double end compaction type) to get φ10 mm and 8-mm-thick pellets followed by degassing at 400 °C for 1 h and sintering at 525 °C for 6 h. The density of the sintered pellets was determined precisely using Archimedes principle provided that the estimated error was less than 1 %. The trimodal microstructure of the bulk composites was examined using optical microscopy (OM), scanning electron microscopy (SEM), and transmission electron microscopy (TEM). The compression test specimens of 4.0 mm× 4.0 mm×8.0 mm are cut from the sintered pellets, and the uniaxial compression tests were performed with a cross head velocity of 1 mm/min. Vickers microhardness tests were also performed using 25 g (25 s) in NC and CG regions separately on the polished and chemically etched surfaces. An average of 15 readings over three independent measurements was used for investigation of hardness values.

3 Results and discussion

3.1 XRD and TEM analysis of Al 6061-10 % TiO_2 nanocomposite powder

Structural characterization using X-ray line broadening analysis can be used to characterize the MAed powders in terms of crystallite size and lattice strain [28]. The crystallite size and lattice strain were estimated by analyzing the broadening of XRD peaks using standard Williamson-Hall formula [25, 29]. Figure 3 shows the XRD patterns of AA 6061-10 wt.% TiO_2 particulate composite powders as function of milling time (0, 1, 5, 10, 20, 30, and 40 h). It can be clearly observed from Fig. 3 that structural changes like some of the peak disappearances, peak broadening, and peak shift occur in the powders with milling time. The peaks of Al, Si, Fe, Cu, and Mg related to AA 6061 Al alloy composition and peaks of TiO_2 were observed during 0 h milling. The minor peaks (Si, Fe, Cu, and Mg) related to alloy constituents disappeared after 10 h of milling, leaving the characteristics of AA 6061 Al alloy formation. Although the intensity of hard TiO_2 particle diffraction peaks decreased by time slightly and even after 40 h of

Table 1 Chemical composition and powder size used to make AA 6061 Al alloy matrix

Name of the element(s)	Purity, %	Element concentration (gravimetric, wt.%)	Powder size, μm (mesh size)
Silicon, Si	99.3	0.600	−45 (<325)
Iron, Fe	99.7	0.700	−75 to +45 (<200 to >325)
Copper, Cu	99.4	0.275	−45 (<325)
Manganese, Mn	99	0.150	−75 to +45 (<200 to >325)
Magnesium, Mg	99.7	1.000	−75 to +45 (<200 to >325)
Chromium, Cr	99.8	0.195	−45 (<325)
Zinc, Zn	99.4	0.250	−45 (<325)
Titanium, Ti	99.3	0.150	−45 (<325)
Aluminum, Al	99.7	Bal	−45 (<325)

Fig. 2 The morphology of as-received powders: **a** Al and **c** TiO$_2$. XRD patterns of as-received powders: **b** Al and **d** TiO$_2$
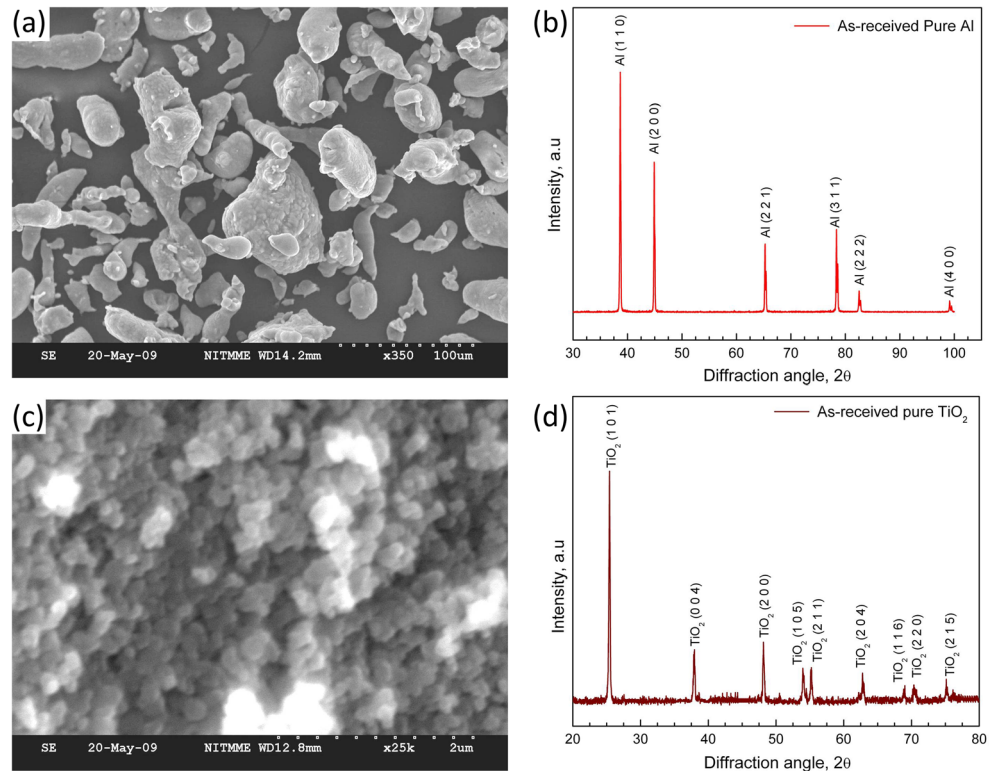
milling, there was no disappearance of peaks corresponding to TiO$_2$ particles. These results indicate that solid solution/dissolution or amorphization of ceramic phase on the soft alloy matrix had not occurred. However, the average clustered TiO$_2$ particle size was reduced to individual particles in nanometer size (119 nm), which was evidenced and discussed elsewhere [21]. Further, the hard TiO$_2$ particles become

Fig. 3 XRD patterns of AA 6061-10 wt.% TiO$_2$ composite powder after 0, 1, 5, 10, 20, 30, and 40 h of milling. *Inset* shows the initial sharp diffraction peaks of Al getting broadened and reduced in intensity

embedded in ductile Al alloy matrix and result in the formation of composite powder particle. The inset of Fig. 3 shows the initial sharp diffraction peaks of Al getting broadened and reduced in intensity because of spatial coherent length confinement [30]. Since slight peak broadening of hard TiO$_2$ particle was observed during milling, the most intensive four TiO$_2$ reflection planes, namely, (1 0 1), (2 0 0), (1 0 5), and (2 1 1), were used to find the crystallite size by peak broadening method. The variation of crystallite size with function of milling time is shown in Fig. 4. It is clear that the crystallite size of Al decreased significantly from around 108 to 48 nm, with an increase in milling time from 1 to 40 h, which indicates that grain refinement occurred in the matrix. The crystallite size of TiO$_2$ was observed to be around 45 and 43 nm after 1 and 40 h of MA, respectively. This showed the insignificance of milling time over the TiO$_2$ crystallite size. The maximum time of milling was set as 40 h, after which the crystallite size of both matrix and TiO$_2$ ceramic phase was observed to be almost identical irrespective of the vast difference between their melting points. On the other hand, the lattice strain increased considerably with milling time up to 10 h (~0.41 %) due to severe plastic deformation (SPD) engendered from the high-energy ball mill. The SPD brought about a deformed lattice with high dislocation density. With further milling, the lattice strain decreased markedly. This may be attributed to the softening of the grain boundaries (GBs), which meant the reduction in the degree of misorientation angle (i.e., higher angle to
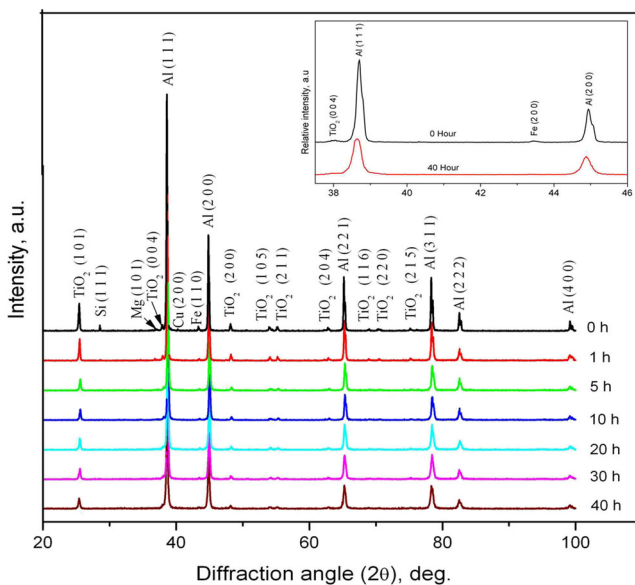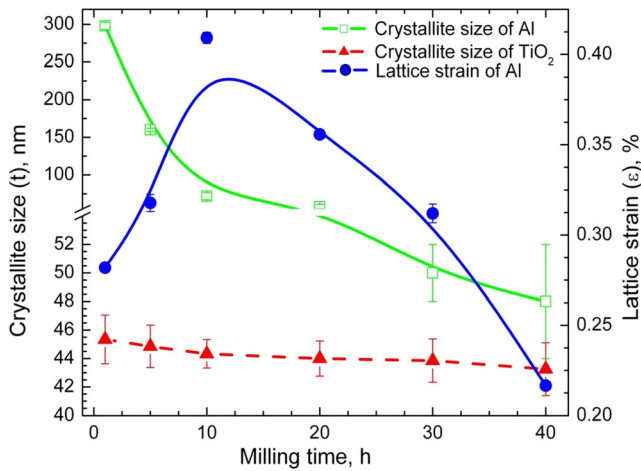
Fig. 4 Variation of crystallite size and lattice strain for AA 6061-10 wt.% TiO_2 composite powder as a function of milling time

lower angle). The decreasing of lattice strain after 15 h was also observed by Tousi et al. [31] with production of Al-20 wt.% Al_2O_3 composite powder by high-energy mechanical milling.

The TEM micrographs of AA 6061_{100-x}-10 wt.% TiO_2 nanocomposite powder are shown in Fig. 5a, d. The matrix crystallite size was calculated based on several bright- and dark-field images, and a minimum of more than 200 grains was counted to get the average grain size. The calculated matrix crystallite size of nanocomposite powders was around 49 nm, respectively. From the selected area of diffraction

(SAD), a continuous sharp ring pattern was observed, which confirmed the nanocrystalline nature of the Al matrix in as-milled (MA, 40 h) condition. The single arrow in the bright-field images of Fig. 5a indicates the TiO_2 particle embedded in the matrix. Further, corresponding EDAX analysis (Fig. 5d) was also performed and tabulated in the respective figures. The presence and embedding of TiO_2 particles in the matrix were confirmed by EDAX spectrum (Fig. 5d), in which the TiO_2 spectrum was observed to increase with percentage of reinforcement.

3.2 Microstructure examination of consolidated trimodaled composites

The optical microstructures of chemically etched trimodal sintered composite are shown in Fig. 6a, d. Two different regions, viz., gray regions and white regions, are observed from the microstructures. The gray region represents NC phase, while the white region represents CG phase of the composite. Homogeneous distribution of ceramic phase and CG phase in NC matrix is very important to get high performance of the trimodal composite. Homogeneous distribution of ceramic phase can be easily achieved via MA, especially for small-sized reinforcement, which can also be used to avoid the cluster formation of reinforcement particles in the matrix [32, 33], even in CNT-reinforced alloy composites [34]. As a result of blending, trimodal composite powders were obtained with good homogenization distribution of CG matrix particles

Fig. 5 TEM micrographs of as milled Al 6061-10 wt.% TiO_2 nanocomposite powders after 40 h of MA: (**a**) bright-field image, (**b**) dark-field image, (**c**) corresponding SAD pattern, (**d**) EDAX analysis. *Single arrow* represents TiO_2 particle

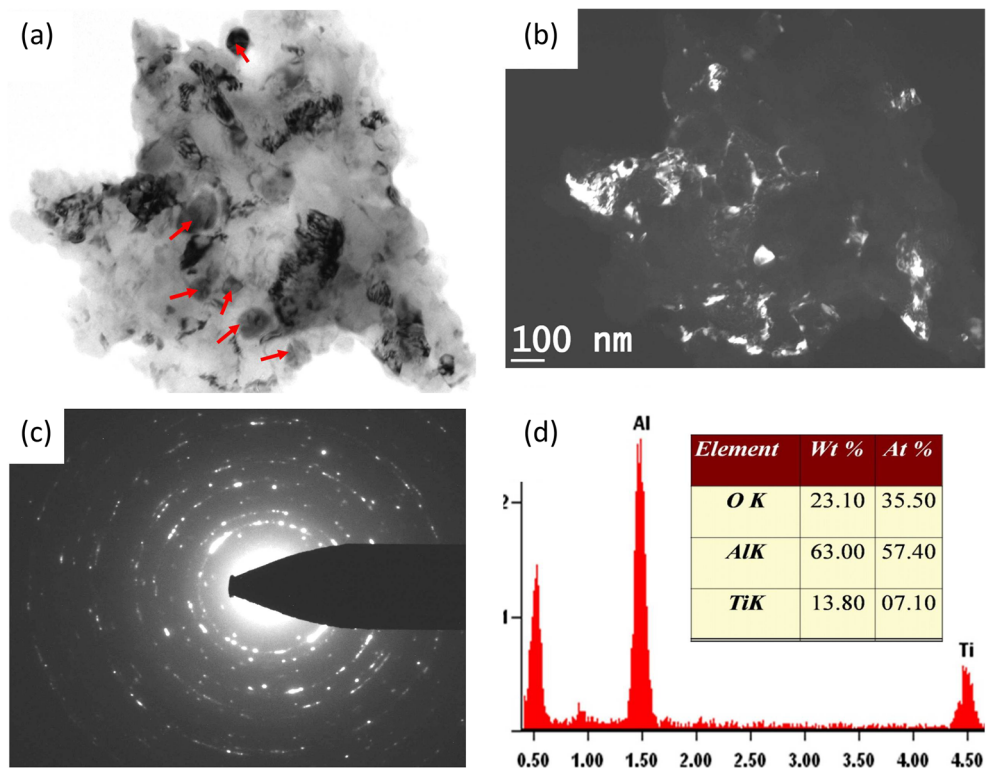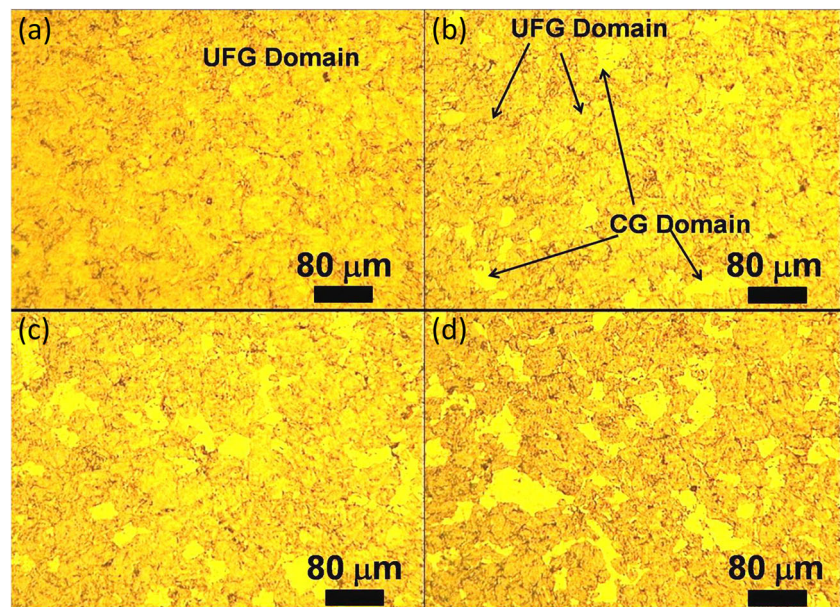| Element	Wt %	At %
O K	23.10	35.50
Al K	63.00	57.40
Ti K	13.80	07.10

Fig. 6 Trimodal microstructures of as-sintered AA 6061-TiO$_2$ composites containing x wt.% CG matrix: **a** x=0 %, **b** x =10 %, **c** x =20 %, and **d** x =30 %. The *gray regions* represent NC matrix reinforced with nano titania; the *bright regions* represent CG matrix

in NC matrix. Figure 6b, d clearly shows the uniform distribution of 10, 20, and 30 % CG matrix in NC matrix. The spacing between the CG bands decreased uniformly as the percentage of CG matrix particles increased. From Fig. 6b, d, it can be observed that as the percentage of CG matrix particles increased, the size of the CG domain also increased. Usually, when the trimodel material is deformed, the dislocations move a significant distance without grain boundary interruption in the coarse grains. Hence, these grains can accommodate a further amount of strain. Hence, the increasing size of CG domain will impart the ductility of the material than the corresponding NC material. The size of the CG band was not increased up to 15 % parent CG phase. The observed average size of CG bands was less than 45 μm up to 15 % parent CG phase. This is due to the non-agglomeration and non-coalescence of individual CG matrix particles. However, the average size of CG bands started to increase beyond 15 %. From Fig. 6d, the 30 % CG sample showed very-large-sized CG bands that evidence the coalescence of individual CG matrix particles. A similar behavior was observed by Witkin et al. [35] while studying the bimodal grain size of Al-Mg alloy (0, 15, and 30 % CG) processed by cryomilling and blending.

To identify the ceramic phase (i.e., third phase) of embedded nano titania particles in NC matrix, detailed backscattered scanning electron image (BSEI) was performed on 0 and 30 % CG matrix in AA 6061-TiO$_2$ nanocomposite, and the same is shown in Fig. 7a, d. The left side of Fig. 7a, c shows the BSEI of the composites at low magnification in which pores and oxide particles were observed. The size of the CG matrix (highlighted for illustrations, Fig. 7c—encircled). Figures 5 and 7c clearly show the large size of the CG band due to coalescence on individual CG matrix particles. The right side

of Fig. 7b, d shows the magnified view of the corresponding composites where the nano-sized titania particles of around 120 nm were completely embedded and uniformly dispersed in the NC matrix. The interface between the CG matrix and NC matrix with TiO$_2$ dispersion was clearly observed from the magnified views of Figs. 5 and 7d. From the OM images and BSEI images, it was clearly observed that the homogeneous distribution of ceramic phase and CG phase in NC matrix was obtained, and that might be useful for getting high performance from the developed trimodal composite.

3.3 TEM analysis of sintered trimodaled composite

Figure 8 shows the bright-field TEM image of 0 % CG AA 6061-TiO$_2$ sintered composite. From Fig. 8, the observed grains of α-Al matrix are almost equiaxed, and nanometer-sized titania particles are uniformly distributed and embedded in the α-Al matrix. The corresponding selected area diffraction (SAD) patterns (inset of upper left of Fig. 8) shows a ring pattern, indicating that the individual grains of α-Al matrix are separated by high-angle grain boundaries and have a random orientation with neighboring grains. Also, the SAD ring pattern reveals that α-Al grains are in ultrafine level. Further, the average grain size of the α-Al matrix is found to be 245±12 nm based on 185 grains counted from the bright-field images of TEM microstructure. The presence of nano-titania dispersoids in the microstructure was distinguished from the diffraction ring patterns. Moreover, the presence of nano-titania particles at grain boundaries explained the stability of grain size at elevated temperatures.

TEM analysis of 15 % CG trimodaled sample is shown in Fig. 9. The presence of CG matrix in UFG matrix embedded with nano-titania particles can be observed from Fig. 9a. The

Fig. 7 BSEI of trimodal AA 6061-TiO$_2$ nanocomposite as a function of CG content: **a, c** 0 and 30 % CG content microstructure; **b, d** magnified view of the corresponding composite
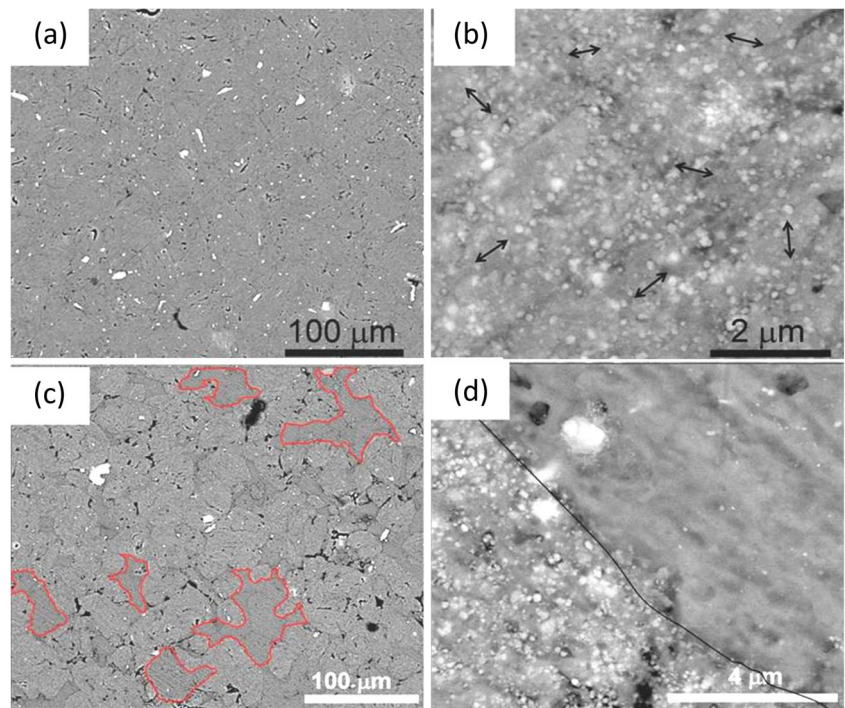
CG matrix consists of equiaxed grains with a size of approximately 1200 nm. The CG matrix can provide more dislocation activities than the NC/UFG matrix. On the other hand, the presence of multiscales (large grains in NC/UFG) in the microstructure may provide attractive combinations of strengths and ductility [18]. From Fig. 9b, it can be clearly observed that the TiO$_2$ particles were not directly exposed to the CG region, there being a thin NC/UFG layer between the reinforcement and CG band. This can be used to load transfer to be more effective. This structure can be explained by the characteristics of MA. As a result of repeated cold welding and fracturing during MA, the TiO$_2$ particles were eventually uniformly distributed in the NC/UFG matrix, with only a few

TiO$_2$ particles that may be observed on the surface of the composite powder [19]. It is well known that a strong metallurgical bond between the reinforcement and the matrix can be obtained via MA. Hence, in the case of trimodaled composite, the effective load transfer can be obtained between the reinforcement and CG matrix by a thin layer of NC/UFG matrix.
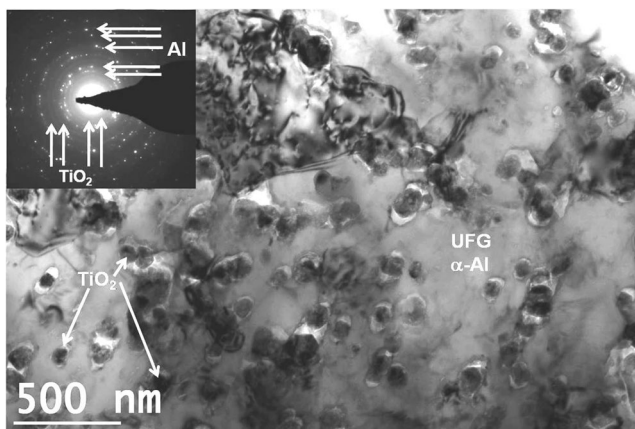

Fig. 8 Bright field image of 0 % CG AA 6061-TiO$_2$ composite showing the nano-sized titania particles embedded in the α-Al matrix. *Inset* at *upper left* shows the corresponding SAD ring pattern indicating UFG nature
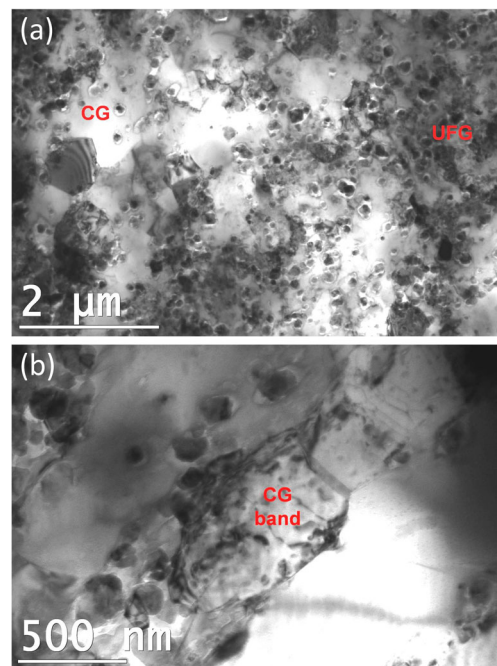

Fig. 9 a Bright-field image of 15 % CG AA 6061-TiO$_2$ trimodaled composite. **b** Magnified view showing the CG band region in 15 % CG trimodaled sample

Table 2 Mechanical properties of trimodal AA 6061-TiO$_2$ nanocomposite

Percentage of CG matrix	Theoretical density (g/cm^3)	Sintered density (g/cm^3)	Relative density	Yield strength at 0.2 % strain, $\sigma_{0.2}$ (MPa)	Strain to failure (%)
0	2.8140	2.5055	0.8904	296.2365	2.2897
5	2.8083	2.5025	0.8911	320.4789	2.7182
10	2.8026	2.5083	0.8950	352.3336	3.4431
15	2.7969	2.5167	0.8998	415.1145	3.8622
20	2.7912	2.5277	0.9056	408.2258	4.9486
25	2.7855	2.5428	0.9129	390.4478	5.6468
30	2.7798	2.5534	0.9185	372.8596	6.1236

3.4 Mechanical property evaluation

The evaluation of mechanical properties of trimodal composites was carried out by conducting room temperature simple uniaxial compression tests. The mechanical properties in terms of theoretical, sintered, and relative densities and yield strength at 0.2 % strain are presented in Table 2. From Table 2, it was clearly observed that the sintered density of the composite increased as the percentage of CG phase increased. This was attributed to the fact that the composites become softer by the addition of CG phase. The stress–strain curves obtained from compression tests of 0, 5, 15, and 30 % CG trimodal-sintered composites are shown in Fig. 10. Inspection of the curves explained that there was a poor strain hardening with engineering strain of approximately 2.2 % only for 0 % CG composite, which meant that it possessed poor ductility [35], but it exhibited yield strength of 296 MPa only, which is a lesser value as compared to all other conditions. The poor ductility of 0 % CG composite might be attributed to the segregation of impurities produced by Ma and interface decohesion of NC matrix and reinforcement. The compressive

strength of 5, 10, 15, 20, 25, and 30 % CG composites were 320, 352, 415, 408, 390, and 372 MPa, respectively. These results interestingly show that the compressive strength increased as the CG content increased up to 15 wt.% CG, and then the values decreased on further addition of CG content from 15 to 30 wt.%. In fact, as the CG bands increase in the NC matrix, the CG bands try to accommodate the dislocation mobility. Moreover, the CG bands arrest the crack propagation, which usually occurs in the NC/UFG bands when the NC or UFG composites were subjected to either compressive or tensile loading. The compressive strength of 15 wt.% CG composite increased by 8 % when compared to 0 % CG composites. This was attributed to improved densification of the composite with increasing soft phase in the structure; effective load transfer occurred in the multiscale microstructure and non-coalescence of individual CG particles. It was expected that effective load transfer might be carried out from CG matrix to UFG matrix because a strong interface between the CG matrix and UFG matrix could be obtained in 15 wt.% CG trimodaled composites. These show that most of the applied load was absorbed by the UFG matrix and the titania
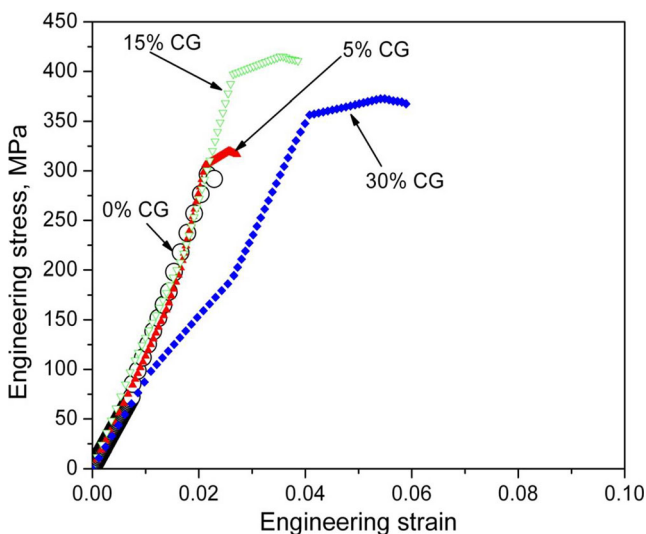

Fig. 10 Room temperature compressive stress–strain curves for sintered trimodal AA 6061-TiO$_2$ nanocomposites
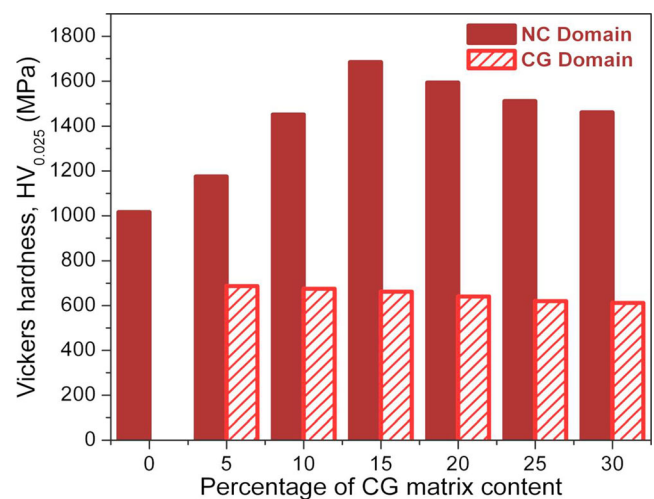

Fig. 11 Vickers microhardness measured from individual nanocrystalline grain and coarse grain of as-sintered trimodal AA 6061-TiO$_2$ nanocomposites

particles, and only a small amount of load remained in the CG matrix. However, on further increasing of CG content in the UFG matrix (i.e., beyond 15 %), the compressive strength started to decrease with increasing soft phase and reduced influence of Hall–Petch effect. This was attributed to the domination of softness of parent CG matrix due to coalescences, and these resulted to a decrease in the effective load transfer rate. When the soft CG matrix was plastically deformed, the dislocation density increases within the grains (CG). These dislocation movements were arrested by the barrier-like grain boundary. Hence, the strain or work hardening takes place. This deformation would be useful for closing the pores to some extent. In contrast, the ductility or work hardening was improved in a better manner. The ductility of 30 % CG trimodal composite was increased over 200 % than 0 % CG composites.

3.5 Microhardness examination on CG and NC domains

Figure 11 shows the Vickers microhardness values of discrete/individual CG and NC domains. The hardness of NC domains increased considerably as the percentage of CG content increased from 0 to 15 %. The low hardness of even NC composite with 0 % parent CG phase was attributed to its low densification, which resulted in more porosity (Fig. 7a; Table 2). The hardness of 15 % CG composites was increased by around 65 % than 0 % CG composites. The increased hardness value for 15 wt.% CG composite was due to non-coalescence of CG band, uniform dispersion of CG band in the NC/UFG matrix, and improved densification (Table 2). Beyond 15 % CG phase, the hardness started to decrease due to coalescence of CG bands in the NC/UFG matrix. Further, the influence of soft phase was observed to be more and resulted in decreased hardness of NC domains. However, the hardness of CG regions was shown to be almost constant irrespective of the fraction of CG phase.

4 Conclusions

Trimodal AA 6061-TiO$_2$ nanocomposite was successfully fabricated, and its microstructural and deformation behavior was investigated. The uniform dispersions of nano-sized titania particles in the NC matrix were achieved via 40 h of MA. Also, uniform distribution of CG bands in NC domains was obtained by blending. The findings can be abridged as follows:

- The 15 % CG trimodal sintered composite exhibited very high yield compressive strength and hardness of 415 MPa and 1.685 GPa, respectively. The reason was expected such that the effective load transfer might be carried out between CG bands to NC domains in 15 % trimodal composites.

- This composite possessed some improvement in the ductility of around 3.86 %. The 30 % CG sintered composites showed high ductility of around 6.12 % but yielded decreased compressive strength and hardness of 372 MPa and 1.462 GPa, respectively.

- The hardness of NC domains increased considerably with increasing fraction of CG phase from 0 to 15 %. The low hardness of even NC composite with lower parent CG phase was attributed to its low densification, which resulted in more porosity. However, beyond 15 % CG phase, decreased hardness of NC domains was observed due to increasing soft phase content.

References

1. Callister, Jr. W.D. Fundamental of material science and engineering, 2nd edn. Wiley, 2007
2. Composite materials hand book, volume 4. Metal matrix composites. Department of Defense, USA, MIL-HDBK-17-4A, 2002, 44–61
3. Varol T, Canakci A (2013) Effect of particle size and ratio of B4C reinforcement on properties and morphology of nanocrystalline Al2024-B4C composite powders. Powder Technol 246:462–472
4. Varol T, Canakci A, Ozsahin S (2013) Artificial neural network modeling to effect of reinforcement properties on the physical and mechanical properties of Al2024-B4C composites produced by powder metallurgy. Compos Part B 54:224–233
5. Wessel, J. K. Handbook of advanced materials enabling new designs. Wiley Interscience, 2004
6. Ramesh CS, Anwar Khan AR, Ravikumar N, Savanprabhu P (2005) Prediction of wear coefficient of Al 6061–TiO$_2$ composites. Wear 259:602–608
7. Troeger LP, Starke EA (2000) Microstructural and mechanical characterization of a superplastic 6xxx aluminium alloy. Mater Sci Eng A 277:102–113
8. Kaczmar JW, Pietrzak K, Wlosinski W (2000) The production and application of metal matrix composite materials. J Mater Process Technol 106(1–3):58–67
9. Varol T, Canakci A (2013) Effect of weight percentage and particle size of B4C reinforcement on physical and mechanical properties of powder metallurgy Al2024-B4C composites. Met Mater Int 19:1227–1234
10. Canakci A, Varol T, Ozsahin S (2013) Prediction of effect of volume fraction, compact pressure and milling time on properties of Al-Al2O3 MMCs using neural networks. Met Mater Int 19:519–526
11. Smagorinski ME, Tsantrizos PG, Grenier S, Cavasin A, Brzezinski T, Kim G (1998) The properties and microstructure of Al-based composites reinforced with ceramic particles. Mater Sci Eng A 244(1):86–90
12. O'Donnell G, Looney L (2001) Production of aluminium matrix composite components using conventional PM technology. Mat Sci Eng A 303:292–301
13. Ramesh CS, Ahmed RN, Mujeebu MA, Abdullah MZ (2009) Fabrication and study on tribological characteristics of cast copper–TiO$_2$–boric acid hybrid composites. Mater Des 30:1632–1637
14. Fan L, Dongmei J, Xueming M (2009) The effect of milling atmospheres on photocatalytic property of Fe-doped TiO$_2$ synthesized by mechanical alloying. J Alloys Compd 470:375–378

15. Suryanarayana C (2001) Mechanical alloying and milling. Prog Mater Sci 46:1–184

16. Varol T, Canakci A (2013) Synthesis and characterization of nanocrystalline Al 2024-B4C composite powders by mechanical alloying. Philos Mag Lett 93:339–345

17. Canakci A, Varol T, Cuvalci H, Erdemir F, Ozkaya S, Yalcın ED (2014) Synthesis of novel CuSn10-graphite nanocomposite powders by mechanical alloying. Micro & Nano Letters 9:109–112

18. Koch CC, Morris DG, Lu K, Inoue A (1999) Ductility of nanostructured materials. MRS Bull 24(2):54–58

19. Han BQ, Lee Z, Nutt SR, Lavernia EJ, Mohamed FS (2003) Mechanical properties of an ultrafine-grained Al-7.5 Pct Mg alloy. Metall Mater Trans A 34A:603–613

20. Kumai KS, Swygenhoven HV, Suresh S (2003) Mechanical behavior of nanocrystalline metals and alloys. Acta Mater 51(19):5743–5774

21. Lee Z, Witkin DB, Radmilovic V, Lavernia EJ, Nutt SR (2005) Bimodal microstructure and deformation of cryomilled bulk nanocrystalline A-7.5 Mg alloy. Mater Sci Eng A 410–411:462–467

22. Han BQ, Lee Z, Witkin D, Nutt S, Lavernia EJ (2005) Deformation behavior of bimodal nanostructured 5083 Al alloys. Metall Mater Trans A 36A:957–965

23. Ye J, Han BQ, Lee Z, Ahn B, Nutt SR, Schoenung JM (2005) A trimodal aluminium based composite with super-high strength. Scr Mater 53:481–486

24. Yao B, Hofmeister C, Patterson T, Sohn Y-H, Bergh MVD, Delahanty T, Cho K (2010) Microstructural features influencing the strength of trimodal aluminum metal-matrix-composites. Compos Part A 41(8):933–941

25. Sivasankarana S, Sivaprasad K, Narayanasamy R, Iyer VK (2010) Synthesis, structure and sinterability of 6061 AA100−x–x wt.% TiO$_2$ composites prepared by high-energy ball milling. J Alloys Compd 491:712–721

26. Witkin DB, Lavernia EJ (2006) Synthesis and mechanical behavior of nanostructured materials via cryomilling. Prog Mater Sci 51(1):1–60

27. Lucadamo G, Yang NYC, San Marchi C, Lavernia EJ (2006) Microstructure characterization in cryomilled Al 5083. Mater Sci Eng A 430(1–2):230–241

28. Löffler J, Weissmüller J (1995) Grain-boundary atomic structure in nanocrystalline palladium from X-ray atomic distribution functions. Phys Rev B Condens Matter 52(10):7076–7093

29. Williamson GK, Hall WH (1953) X-ray line broadening from filed aluminium and wolfram. Acta Metal 1:22–31

30. Kumaran S, Sasikumar T, Arockiakumar R, Srinivasa Rao T (2008) Nanostructured titanium aluminides prepared by mechanical alloying and subsequent thermal treatment. Powder Technol 185(2):124–130

31. Razavi-Tousi SS, Yazdani Rad R, Salahi E, Mobasherpour I, Razavi M (2009) Production of Al–20 wt.% Al$_2$O$_3$ composite powder using high energy milling. Powder Technol 192:346–351

32. Zhou F, Liao XZ, Zhu T, Dallek S, Lavernia EJ (2003) Microstructural evolution during recovery and recrystallization of a nanocrystalline Al-Mg alloy prepared by cryogenic ball milling. Acta Mater 51(10):2777–2791

33. Sivasankarana S, Sivaprasad K, Narayanasamy R, Iyer VK (2010) An investigation on flowability and compressibility of AA 6061100−x-x wt.% TiO$_2$ μ and nanocomposite powder prepared by blending and mechanical alloying. Powder Technol 201:70–82

34. Pérez-Bustamante R, Estrada-Guel P, Amézaga-Madrid M, Miki-Yoshida JM, Herrera-Ramírez, Martínez-Sánchez R (2010) Microstructural characterization of Al-MWCNT composites produced by mechanical milling and hot extrusion. J Alloys Compd 495:399–402

35. Witkin D, Lee Z, Rodriguez R, Nutt S, Lavernia EJ (2003) Al-Mg alloy engineered with bimodal grain size for high strength and increased ductility. Scr Mater 49:297–302